IEEE Photonics Journal
An IEEE Photonics Society Publication

Open Access

Mode Investigation for Hybrid Microring Lasers With Sloped Sidewalls Coupled to a Silicon Waveguide

Volume 7, Number 2, April 2015

Shao-Shuai Sui
Ming-Ying Tang
Yue-De Yang
Jin-Long Xiao
Yun Du
Yong-Zhen Huang, Senior Member, IEEE

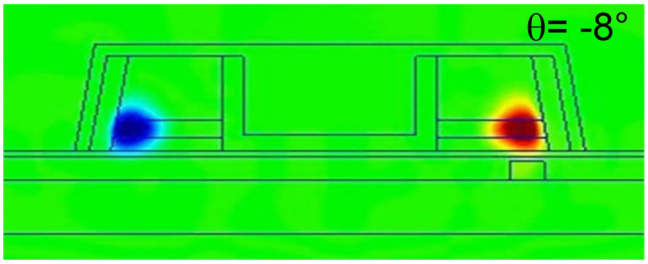

DOI: 10.1109/JPHOT.2015.2416119
1943-0655

IEEE photonics SOCIETY

IEEE

Mode Investigation for Hybrid Microring Lasers With Sloped Sidewalls Coupled to a Silicon Waveguide

Shao-Shuai Sui, Ming-Ying Tang, Yue-De Yang, Jin-Long Xiao, Yun Du, and Yong-Zhen Huang, *Senior Member, IEEE*

State Key Laboratory on Integrated Optoelectronics, Institute of Semiconductors, Chinese Academy of Sciences, Beijing 100083, China

DOI: 10.1109/JPHOT.2015.2416119

Manuscript received February 5, 2015; revised March 16, 2015; accepted March 20, 2015. Date of publication March 23, 2015; date of current version April 8, 2015. This work was supported in part by the NSFC/RGC joint project under Grant 61431166003 and in part by the High Technology Project of China under Grant 2012AA012202. Corresponding author: Y.-Z. Huang (e-mail: yzhuang@red.semi.ac.cn).

Abstract: Hybrid AlGaInAs/InP microring lasers with sloped sidewalls coupled to a silicon waveguide are investigated numerically and experimentally. The mode field distribution deviations for the microring resonator with the sloped sidewalls at different tilting angles are simulated by a 3-D finite-difference time-domain technique. Obvious enhancements of output coupling to the silicon waveguide and the active region optical confinement factor can be expected as the microresonator has a trapezoidal shape. A hybrid microring laser with a radius of 19 μm and a width of 2 μm is fabricated with the laser wafer bonded on a silicon-on-insulator wafer using the divinylsiloxane-benzocyclobutene (DVS-BCB) adhesive bonding technique. Continuous-wave electrically injected operation is realized at a tilting angle of -6° with the threshold currents of 7.8 and 9 mA at 12 °C and 22 °C. In addition, for a hybrid microring laser with a radius of 29 μm and a ring width of 2.5 μm, continuous-wave electrical operation up to 50 °C is achieved.

Index Terms: Microcavities, optical resonators, semiconductor lasers, lasers bonded on SOI.

1. Introduction

Silicon photonics have been put on agenda for meeting the requirements of large-scale photonic integration due to the high index contrast with silica and compatible with complementary metal oxide semiconductor (CMOS) process [1], [2], and silicon based functional passive devices have been extensively investigated, such as filters [3], switches [4], modulators [5], and buffers [6]. A low-power consumption light source on silicon is essential in the photonic integration circuits, however, silicon based lasers are difficult to achieve due to the indirect band gap and poor emission efficiency [7], [8]. The hybrid integration of III-V materials on silicon and silicon-on-insulator (SOI) through die-to-wafer bonding techniques have attracted great attention to realize hybrid silicon lasers for the photonic integration, such as direct molecular bonding technique [9], [10], divinylsiloxane-benzocyclobutene (DVS-BCB) adhesive bonding technique [11], [12], and metal bonding technique [13]. Hybrid microdisk and microring lasers with the merits of small footprint and low threshold were demonstrated by the hybrid integration techniques [14]–[16]. Recently,

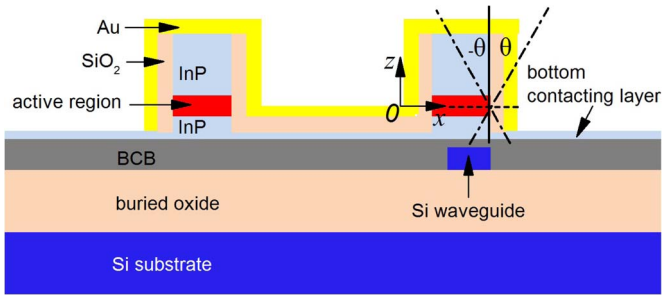

Fig. 1. Cross section view of the 3-D microring lasers used in the simulation. The dashed-dotted lines indicate the tilting angle θ.

we have demonstrated a sixteen-wavelength hybrid microdisk laser array adhesively bonded on a SOI silicon waveguide with a channel spacing about 3 nm [17]. In a micro-disk or ring resonator, the light propagates around the periphery of the resonator via the total internal reflection. For the InP-based microlasers with sloped sidewalls, the quality factor and optical confinement factor will dramatically decrease due to the large radiation loss to the substrate, which leads to a high threshold operation and low output coupling efficiency [18]. However, for the hybrid microdisk and microring lasers bonded on SOI, vertically strong waveguiding will limit the vertical radiation loss.

In this paper, the sloped angles of resonator sidewalls are designed to improve the performance of the hybrid microlasers. The mode characteristics are firstly investigated for the hybrid microring lasers with sloped sidewalls using the three-dimensional (3-D) finite-difference time-domain (FDTD) method. Obvious enhancements of waveguide output coupling efficiency and the optical confinement factor are obtained as the tilting angle of microring resonator is less than 0. Then hybrid AlGaInAs/InP microring lasers vertically coupled to a SOI silicon waveguide are fabricated using the standard photolithography and DVS-BCB adhesive bonding techniques. Continuous-wave electrical operations with the threshold currents of 7.8 and 9 mA are realized at 12 and 22 °C, respectively, for a hybrid microring laser with a radius of 19 μm and a width of 2 μm, and the sloped tilting angle of $-6°$. For a hybrid microring laser with a radius of 29 μm and the ring width of 2.5 μm, continuous-wave electrical operation up to 50 °C is achieved.

2. Mode Simulation for the Hybrid Microring Lasers With Sloped Sidewalls

In this section, the mode characteristics of a small size microring resonator are investigated for the transverse electric (TE) modes by 3D FDTD technique using the Rsoft FullWAVE package. For the 3D microring resonator with the cross-sectional view as in Fig. 1, we consider the influence of the tilting angle θ on the mode characteristics for the resonator with the radius at the middle of active region of 3 μm and the microring width of 1.5 μm. The simulated cavity size is mainly limited by the computation power of our computing system. The thicknesses of the upper-and lower-InP cladding layers, the active region, BCB layer and buried oxide layer are 1.2, 0.35, 0.3, 0.45, and 1 μm, respectively, following the practical lasers. The width and height of the silicon waveguide are taken to be 500 nm and 350 nm. The refractive indices of the InP layer, the active region, the BCB layer and the silicon waveguide are 3.14, 3.4, 1.54 and 3.48, respectively [19]. The thicknesses of the insulating layer SiO_2 and the gold electrode layer are taken to be 300 nm and 200 nm, with the refractive indices of 1.45 and $0.18 + i10.2$, respectively. The n-InP cladding layer in the external region of the microring resonator is etched to leave a layer thickness of 100 nm as the bottom contacting layer.

In the simulation, a mesh with a cell size of 40 nm in the x and y directions and a cell size of 25 nm in the z direction are used, and perfectly matched layer (PML) absorbing boundary conditions are applied to terminate the FDTD computation window. Firstly, a Gaussian modulated cosine exciting source $P(t) = \exp[-(t - t_0)^2/t_w^2]\cos(2\pi f_0 t)$ is used inside the microring resonator, with the half-width of the pulse $t_w = 5.167$ fs, pulse center $t_0 = 2t_w$, and center frequency

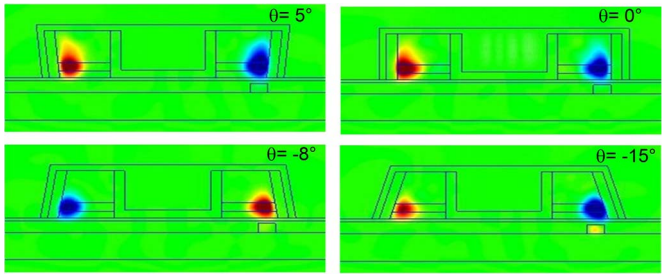

Fig. 2. Cross-sectional field patterns of magnetic component H_z at $y = 0$ for the mode $TE^0_{1,37}$ at the tilting angle θ of 5°, 0, −8°, and −15° in a microring with a radius of 3 μm and a ring width of 1.5 μm.

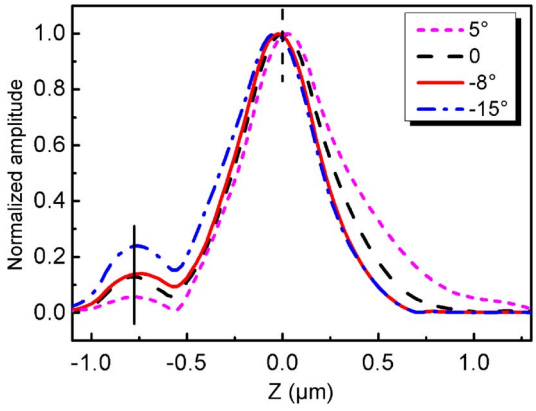

Fig. 3. Normalized field amplitudes for the mode $TE^0_{1,37}$ are plotted at $\theta = 5°$, 0, −8°, and −15°, respectively, for a microring with a radius of 3 μm and a ring width of 1.5 μm. The solid and dashed vertical lines indicated the middle positions of the silicon waveguide and active region.

$f_0 = 193.5$ THz to excite multiple modes over a wide frequency range. Then, mode intensity spectra are calculated using the Padé approximation [20], and a narrowband pulsed exciting source centered at the mode resonate frequency of 210 THz with $t_w = 833.3$ fs and $t_0 = 2t_w$ is chosen to simulate the mode field distribution and Q-factor for the mode $TE^0_{1,37}$ according to the mode intensity spectra.

The cross-sectional field patterns of the magnetic field H_z at $y = 0$ are plotted in Fig. 2 for the mode $TE^0_{1,37}$ at $\theta = 5°$, 0, −8°, and −15°, respectively. Obvious deviations of mode field distributions are observed with the sloped sidewalls, which are caused by the change of vertical refractive index distribution. Compared with the field pattern at $\theta = 0$, the mode field mainly distributes in the active region and n-InP layer as $\theta < 0$, and a high coupling output efficiency and a large optical confinement factor can be obtained simultaneously. For $\theta > 0$, a large mode tail in the thick up-cladding p-InP layer is observed, which will cause a large absorption loss in the heavily p-doped and narrow bandgap InGaAs ohm contacting layer. The normalized field amplitudes in the z direction for the mode $TE^0_{1,37}$ are shown in Fig. 3 at $\theta = 5°$, 0, −8°, and −15° and $r = 2.75$ μm, respectively, where the center positions of the silicon waveguide and the active region are indicated by the solid and dotted vertical lines. The position of the maximum field distribution deviates from the middle of the active region to the silicon waveguide of 25, 25, and 50 nm as $\theta = 5°$, −8°, and −15°, respectively.

The Q-factors and the mode frequency versus the tilting angle θ are plotted in Fig. 4(a) for the mode $TE^0_{1,37}$ in the microring resonators with and without the underlying silicon waveguide,

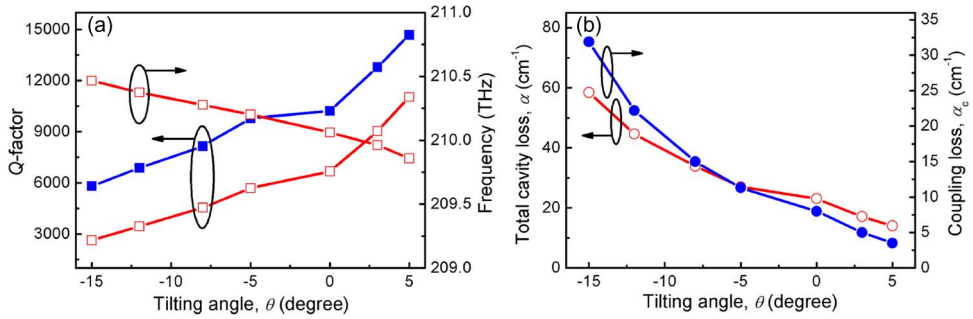

Fig. 4. (a) Mode Q-factors with (open squares) and without (solid squares) the underlying silicon waveguide and the mode frequency versus θ and (b) calculated total cavity loss α (open circles) and waveguide coupling loss α_c (solid circles) versus θ for the mode $TE^0_{1,37}$ in the microring resonator with a radius of 3 μm and a ring width of 1.5 μm.

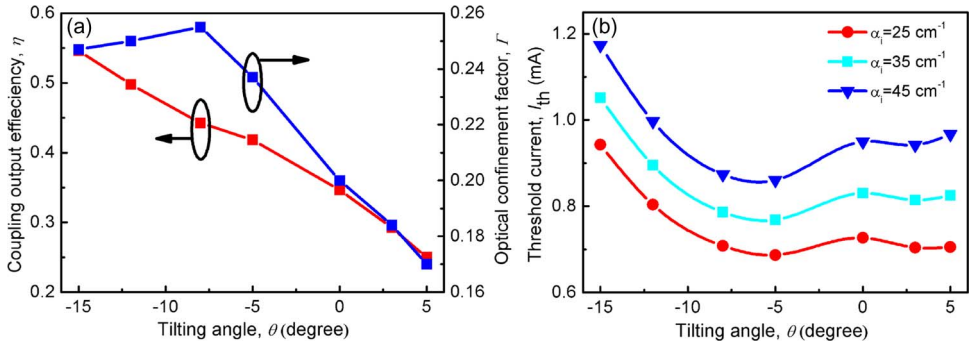

Fig. 5. (a) Calculated waveguide coupling output efficiency η and the quantum well optical confinement factor Γ versus the tilting angle θ, and (b) the calculated threshold current I_{th} versus the tilting angle θ for a microring with a radius of 3 μm and a ring width of 1.5 μm.

respectively. We find that the Q-factor drops as θ decreases due to the increasing coupling loss to the bottom contacting layer and the silicon waveguide. The mode Q-factors for the microring resonator with a silicon waveguide Q_w are 4.2×10^3, 6.7×10^3, and 1.1×10^4 at $\theta = -8^\circ$, 0, and 5°, respectively, and the corresponding mode Q-factors for the microring resonator without a silicon waveguide Q_{wo} are 7.7×10^3, 1×10^4, and 1.5×10^4. According to the relation between the mode Q-factor and the mode loss α of $Q = n_g k_0/\alpha$, where k_0 is the wavenumber in vacuum, $n_g = 3.5$ is the group refractive index [18], and we calculate the total mode loss α versus θ as shown in Fig. 4(b). The waveguide coupling loss α_c shown in Fig. 4(b) is calculated by [21]

$$\alpha_c = k_0 \cdot n_g \cdot \left(\frac{1}{Q_w} - \frac{1}{Q_{wo}}\right). \tag{1}$$

The total mode loss for the microring resonator with the underlying silicon waveguide is 36.4, 23.1, and 14 cm^{-1} at $\theta = -8^\circ$, 0, and 5°, respectively, and the corresponding waveguide coupling loss is 16.5, 8.0, and 3.5 cm^{-1}. The waveguide coupling output efficiency defined as the ratio of α_c to α is plotted as a function of θ in Fig. 5(a) for the mode $TE^0_{1,37}$, with the efficiency of 45.3%, 34.6%, and 25% at $\theta = -8^\circ$, 0, and 5°. In addition, we also consider the microring resonator coupled to a silicon waveguide with a width of 2 μm, and get the output efficiency of 60.7% 50.2%, and 42.6% for the mode $TE^0_{1,37}$ at $\theta = -8^\circ$, 0, and 5° due to the larger coupling region. Furthermore, the quantum well optical confinement factor Γ, defined as the ratio of the mode energy confined in the active region quantum well to the total mode energy, is also shown in

TABLE 1

Calculated quality factor Q, waveguide coupling output efficiency η, and threshold current I_{th} versus the bottom contacting layer thickness d for the mode $TE^0_{1,37}$. (The microring has a radius of 3 μm and a width of 1.5 μm at $\alpha_i = 35$ cm^{-1} and $\theta = -8°$.)

d (nm)	0	50	100	150	200
Q	9071	7164	4550	2476	1911
η	60%	54.7%	44.3%	21.8%	14.9%
I_{th} (mA)	0.66	0.69	0.79	1.06	1.29

Fig. 5(a), which shows the higher optical confinement factor as $\theta < 0$. The quantum well optical confinement factors of 0.17, 0.2, and 0.255 are obtained for the microring resonator with θ of 5°, 0, and $-8°$, respectively.

In order to demonstrate the influence of the sloped sidewalls on the lasing characteristics, we calculate the threshold current for the hybrid microring lasers with the radius of 3 μm and the width of 1.5 μm by [16]

$$I_{th} = \frac{qV}{\eta_i} N_{tr}^2 \left[B + C_{QW} N_{tr} e^{(\alpha_i + \alpha_m)/\Gamma g_0} \right] e^{2(\alpha_i + \alpha_m)/\Gamma g_0} \tag{2}$$

where q is the elementary electric charge, V is the active region volume, N_{tr} is the transparent carrier density, Γ is the quantum well optical confinement factor, g_0 is the quantum well material gain, η_i is the injection efficiency, α_i is the internal modal loss, B is the bimolecular recombination coefficient, C_{QW} is temperature dependent Auger coefficient, and α_m is the cavity outcoupler loss.

The parameters $N_{tr} = 1.9 \times 10^{18}$ cm^{-3}, $g_0 = 900$ cm^{-1}, $\eta_i = 0.6$, $B = 10^{-10}$ cm^3/s, and $C_{QW} = 2.685 \times 10^{-29}$ cm^6/s at 293 K are used in the simulation. The calculated threshold current I_{th} versus θ is plotted in Fig. 5(b) at the different internal loss α_i for the microring lasers with a radius of 3 μm and a width of 1.5 μm. The threshold current decreases with θ from 0 to $-8°$ due to the higher quantum well optical confinement factor, and the corresponding waveguide coupling output efficiency increases from 25% to 45.3%. For $\theta < -8°$, the optical confinement factor varies slowly, and the threshold current increases due to the larger coupling loss to the silicon waveguide. For $5° > \theta > 0$, the threshold current almost keeps constant caused by the balance between the high Q-factor and low optical confinement factor.

Hence, the simulation results indicate that the microring resonator with sloped sidewalls can compel the mode field distribution shift to the silicon waveguide as $\theta < 0$, and enhance coupling output efficiency to the silicon waveguide and optical confinement factor due to the high index contrast with BCB layer. For the tilting angle θ from 0 to $-8°$, the coupling output efficiency increases from 25% to 45.3%, and the lower threshold current is expected simultaneously. In fact, we can adjust the thicknesses of the bottom InP contacting layer thickness, the SiO_2 isolation layer thickness, and the tilting angle to optimize the mode Q-factor and the output-coupling efficiency. The simulated Q-factor, waveguide coupling output efficiency η and threshold current I_{th} are summarized in Table 1 for the microring resonator with a radius of 3 μm and a width of 1.5 μm at $\alpha_i = 35$ cm^{-1} and $\theta = -8°$, and the bottom contacting layer thickness $d = 0$, 50, 100, 150, and 200 nm, for the mode $TE^0_{1,37}$. As d decreases from 200 to 0 nm, the Q-factor increases from 1911 to 9071, corresponding coupling output efficiency also increases from 14.9% to 60%, and the threshold current reduces from 1.29 to 0.66 mA. Therefore, the high output efficiency and low threshold current can be expected simultaneously by improving the structure design.

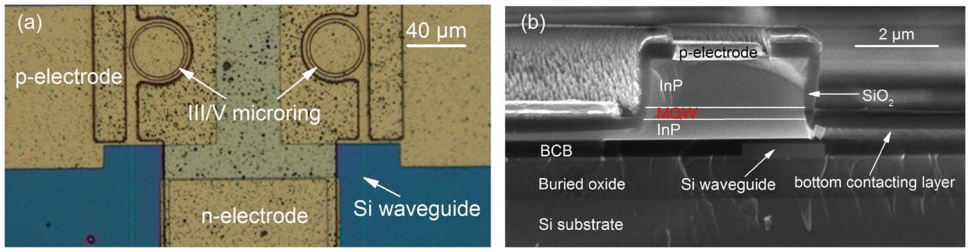

Fig. 6. (a) Top-view microscope image of two hybrid microring lasers covered with p-electrode metallic layer. (b) Cross-sectional-view SEM image of the InAlGaAs/Si microring laser coupled to a silicon waveguide with the sloped tilting angle of $-6°$.

3. Fabrication Processes

The hybrid microring laser is fabricated using an AlGaInAs/InP laser wafer grown on a p-InP substrate by metal-organic chemical vapor deposition. The laser wafer comprises an InGaAsP etch-stop layer, a 0.1 μm $p - In_{0.53}Ga_{0.47}As$ as the p-electrode contacting layer, a 1.2 μm p-InP cladding layer, eight compressively strained AlGaInAs quantum wells with the well thickness of 5 nm and the barrier thickness of 9 nm sandwiched between two 90 nm AlGaInAs separated confined layers, and a 0.35 μm n-InP as the cladding and n-electrode contacting layer.

The AlGaInAs/InP laser wafer is bonded on a patterned SOI wafer with silicon optical waveguides using DVS-BCB Cyclotene 3022-35. The SOI optical waveguides are formed in the SOI wafer with a 360 nm top-silicon and a 1-μm buried oxide (BOX). The simple cleanings are performed for SOI wafer, and the adhesion promoter solution is spin-coated on the SOI wafer to improve the adhesion of the polymer. Then the DVS-BCB solution is spin-coated onto the SOI wafer, and the BCB thickness upon the silicon waveguide is less than 100 nm in order to keep high coupling output efficiency to the silicon waveguide. After that, the SOI substrate is baked for 15 min at 140 °C to remove the solvents, and the laser wafer die at a size of 1×1 cm^2 is bonded on the SOI wafer. The bonded wafer is annealed at 250 °C for 1 hour in a N_2 atmosphere. Finally the bonded laser wafer is slowly cooled down to room temperature, and the p-InP substrate is removed by physically grinding and chemical etching processes, with a 3:1 HCl/H_2O solution to remove the InP substrate and a 3:1:1 $H_2SO_4/H_2O_2/H_2O$ solution to etch the InGaAsP etch-stop layer.

The fabrication processes of hybrid microring lasers are summarized as follows. Firstly, a 500 nm SiO_2 layer is deposited on the bonded laser wafer by plasma enhanced chemical vapor deposition (PECVD). The microring resonator patterns are transferred onto the SiO_2 layer using standard contacting photolithography technique. Then, the patterned SiO_2 layer is used as a hard mask to etch the AlGaInAs/InP laser wafer with a total etching depth of about 1.7 μm to the bottom contacting layer by inductively coupled plasma (ICP) etching process. Subsequently, HF solution is used to remove the residual SiO_2 hard mask with the microring patterns in the laser wafer. Thirdly, an Au-Ge-Ni n-electrode layer away from the microring resonator of about 2 μm is deposited by electron-beam evaporation and lift-off techniques. After that, a 300 nm SiO_2 insulating layer is deposited by PECVD on the wafer. Finally, a p-type contact window is etched on top of the microring resonator, and a Ti-Pt-Au p-electrode is deposited, totally covering the microring resonator to improve the thermal characteristics. The top-view microscope image of two hybrid microring lasers covered by the p-electrode metallic layer is shown in Fig. 6(a), and the scanning-electron microscope (SEM) image of the cross-sectional hybrid microring resonator with sloped tilting angle of about $-6°$ is displayed in Fig. 6(b). The underlying Si rib waveguide has a etch depth of 300 nm, a width of 2 μm, and a 40-nm-thick outer slab. The BCB thickness above the Si rib waveguide is about 100 nm, and the bottom contacting InP layer thickness is about 150 nm.

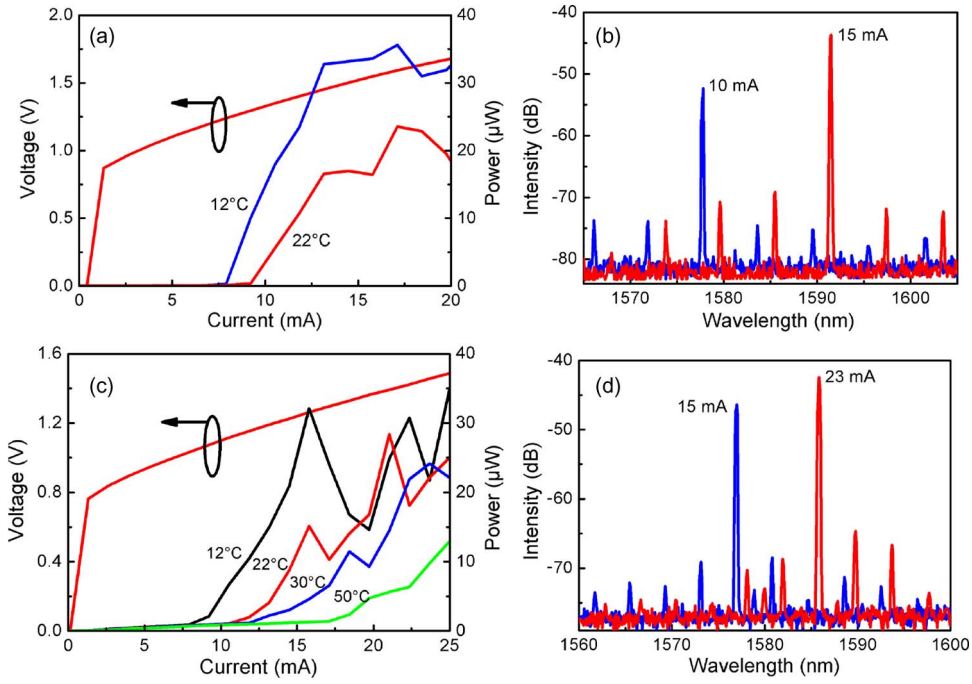

Fig. 7. (a) Output powers from the silicon waveguide and applied voltage versus CW injection current, and (b) lasing spectra at continuous injection currents of 10 mA and 15 mA at the TEC temperature of 22 °C for a hybrid microring laser with a radius 19 μm and a width of 2 μm. (c) Output powers and applied voltage versus CW injection current at 12, 22, 30, and 50 °C, and (d) lasing spectra at CW injection currents of 15 mA and 23 mA at 22 °C, for a hybrid microring laser with a radius 29 μm and a ring width of 2.5 μm.

4. Output Characteristics of Hybrid Microring Lasers Coupled to a Silicon Waveguide

The hybrid microring lasers with the p-side up are bonded on a thermoelectric cooler (TEC) after cleaving the silicon waveguide. For an AlGaInAs/Si microring laser with a radius of 19 μm and a ring width of 2 μm, the output powers versus continuous-wave (CW) injection currents are shown in Fig. 7(a) at the TEC temperatures of 12 °C and 22 °C. The output powers are measured through a multi-mode fiber positioned near the cleaved silicon waveguide end face. The corresponding threshold currents are 7.8 and 9 mA and the maximum output powers are 36 and 24 μW, respectively, at 12 and 22 °C. The threshold current density is 3.45 kA/cm^2 at 12 °C, and a series resistance of 43 Ω is estimated from the voltage-current curve at 22 °C in Fig. 7(a). Besides, the abrupt kinks are observed in the output power-injection current curves, which are caused by the mode jumps as well as mode competition between the clockwise and the counter-clockwise propagating modes. The lasing spectra at CW injection currents of 10 and 15 mA are measured and plotted in Fig. 7(b) at the TEC temperature of 22 °C. Single mode operation with the side-mode-suppression ratios (SMSR) of 21.5 and 25.5 dB is obtained at 10 and 15 mA, with the main lasing mode jumping from 1577.79 nm to 1591.49 nm and a thermal-induced mode wavelength shift about 1.8 nm. The mode wavelength shift versus the dissipated power is about 0.19 nm/mW based on the applied electric power. Considering the lasing mode wavelength redshift rate of 0.1 nm/K, we expect a temperature rise of about 18 K from 10 to 15 mA and a thermal resistance of 1.9 K/mW. The observed longitudinal mode interval is 5.9 nm at 1585 nm, which corresponds to a group index of 3.6.

For a hybrid microring laser with the radius of 29 μm and the ring width of 2.5 μm, Fig. 7(c) shows the measured output powers versus CW injection currents. The threshold currents are 7.8, 10.6, 11.8, and 17.1 mA, respectively, at the TEC temperatures of 12, 22, 30, and 50 °C,

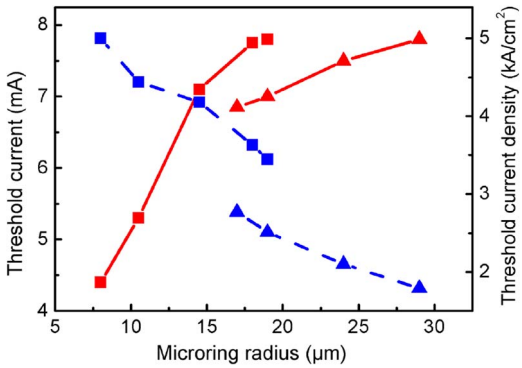

Fig. 8. Threshold current (solid lines) and threshold current density (dashed lines) versus microring radius at 12 °C. (The squares represent the microring width of 2 μm, and triangles are for the 2.5-μm-width microring.)

and the threshold current density is 1.79 kA/cm^2 at 12 °C. The maximum output powers are 35 and 13 μW at the TEC temperatures of 12 and 50 °C, respectively. A series resistance of 28 Ω is calculated according to the voltage-current curve at 22 °C in Fig. 7(c). The lasing spectra at CW injection currents of 15 and 23 mA and TEC temperature of 22 °C are plotted in Fig. 7(d). From 15 to 23 mA, the main lasing mode jumps from 1576.98 nm to 1585.85 nm with the SMSR of 22 dB, and a thermal-induced mode wavelength shift of 1.1 nm is obtained. The mode wavelength shift versus the dissipated electric power is 0.075 nm/mW, and a thermal resistance of 0.75 K/mW and a temperature rise of 11 K are estimated from 15 to 23 mA.

Finally, the threshold currents and threshold current densities for the hybrid microring lasers with the ring widths of 2 μm and 2.5 μm are summarized in Fig. 8 as the functions of microring radius at 12 °C, respectively. For the microring radius of 8 μm and the width of 2 μm, the CW lasing is achieved with the threshold current of 4.4 mA corresponding to the threshold current density of 5 kA/cm^2. As the microring radius increases to 19 μm, the threshold current density decreases to 3.45 kA/cm^2, due to the higher mode *Q*-factor. Obvious reductions of threshold current density and threshold current are observed for the microring width of 2.5 μm, mainly caused by relatively low radiation loss. The large threshold current density is attributed to the low quality factor caused by radiation loss through the thick bottom n-InP contacting layer, and therefore, the precise etching process is needed to improve the output characteristics. For the microring laser with a radius of 19 μm and a width of 2 μm, the active region volume is 10.7 times the microring structure used in Table 1. The corresponding threshold current in Fig. 8 is also about 10 times the simulated value in Table 1.

5. Conclusion

In conclusion, we have proposed and demonstrated a hybrid silicon AlGaInAs/InP microring laser with the sloped sidewalls, and the mode characteristics are investigated by the 3-D FDTD technique. The mode field pattern deviations caused by the sloped sidewalls are studied, and the enhancements of waveguide coupling output efficiency and low threshold operation are expected with a tilting angle of about $-6°$. The hybrid microring lasers with the sloped sidewalls are fabricated using DVS-BCB bonding technique, and continuous-wave electrically injected lasing with the threshold current of 7.8 and 9 mA is obtained for a microring laser with a radius of 19 μm and a width of 2 μm at 12 and 22 °C. For a hybrid microring laser with a radius of 29 μm and a ring width of 2.5 μm, continuous-wave electrical operation up to 50 °C is achieved.

Acknowledgment

The authors thank Prof. A. W. Poon and Nanoelectronics Fabrication Facility (NFF) of HKUST for support in the fabrication of silicon waveguides.

References

[1] M. J. R. Heck *et al.,* "Hybrid silicon photonics for optical interconnects," *IEEE J. Sel. Topics Quantum Electron.*, vol. 17, no. 2, pp. 333–346, Mar./Apr. 2011.

[2] D. A. B. Miller, "Device requirements for optical interconnects to silicon chips," *Proc. IEEE*, vol. 97, no. 7, pp. 1166–1185, Jul. 2009.

[3] P. Dong *et al.,* "Thermally tunable silicon racetrack resonators with ultralow tuning power," *Opt. Exp.*, vol. 18, no. 19, pp. 20298–20304, Sep. 2010.

[4] A. W. Poon, X. S. Luo, F. Xu, and H. Chen, "Cascaded microresonator-based matrix switch for silicon on-chip optical interconnection," *Proc. IEEE*, vol. 97, no. 7, pp. 1216–1238, Jul. 2009.

[5] D. J. Thomson *et al.,* "High contrast 40Gbit/s optical modulation in silicon," *Opt. Exp.*, vol. 19, no. 12, pp. 11507–11516, Jun. 2011.

[6] F. Xia, L. Sekaric, and Y. Vlasov, "Ultracompact optical buffers on a silicon chip," *Nat. Photon.*, vol. 1, no. 1, pp. 65–71, Jan. 2007.

[7] R. E. Camacho-Aguilera *et al.,* "An electrically pumped germanium laser," *Opt. Exp.*, vol. 20, no. 10, pp. 11316–11320, May 2012.

[8] H. Y. Liu *et al.,* "Long-wavelength InAs/GaAs quantum-dot laser diode monolithically grown on Ge substrate," *Nat. Photon.*, vol. 5, no. 7, pp. 416–419, Jul. 2011.

[9] X. Sun *et al.,* "Electrically pumped hybrid evanescent Si/InGaAsP lasers," *Opt. Lett.*, vol. 34, no. 9, pp. 1345–1347, May 2009.

[10] Y. J. Zhang *et al.,* "Hybrid III-V/silicon single-mode laser with periodic microstructures," *Opt. Lett.*, vol. 38, no. 6, pp. 842–844, Mar. 2013.

[11] S. Keyvaninia *et al.,* "Heterogeneously integrated III-V/silicon distributed feedback lasers," *Opt. Lett.*, vol. 38, no. 24, pp. 5434–5437, Dec. 2013.

[12] S. Stankovic *et al.,* "Hybrid III-V/Si distributed-feedback laser based on adhesive bonding," *IEEE Photon. Technol. Lett.*, vol. 24, no. 23, pp. 2155–2158, Dec. 2012.

[13] L. J. Yuan *et al.,* "Hybrid InGaAsP-Si evanescent laser by selective-area metal-bonding method," *IEEE Photon. Technol. Lett.*, vol. 25, no. 12, pp. 1180–1183, Jun. 2013.

[14] P. Mechet *et al.,* "Uniformity of the lasing wavelength of heterogeneously integrated InP microdisk lasers on SOI," *Opt. Exp.*, vol. 21, no. 9, pp. 10 622–10 631, May 2006.

[15] L. Liu *et al.,* "An ultra-small, low-power, all-optical flip-flop memory on a silicon chip," *Nat. Photon.*, vol. 4, no. 3, pp. 182–187, Mar. 2010.

[16] D. Liang, M. Fiorentino, S. Srinivasan, J. E. Bowers, and R. G. Beausoleil, "Low threshold electrically-pumped hybrid silicon microring lasers," *IEEE J. Sel. Topics Quantum Electron.*, vol. 17, no. 6, pp. 1528–1533, Nov./Dec. 2011.

[17] S. S. Sui *et al.,* "Sixteen-wavelength hybrid AlGaInAs/Si microdisk laser array," *IEEE J. Quantum Electron.*, vol. 51, no. 4, Apr. 2015, Art. ID. 2600108.

[18] J. Li, Y. D. Yang, and Y. Z. Huang, "Mode simulation for midinfrared microsquare resonators with sloped sidewalls and confined metals," *IEEE Photon. Technol. Lett.*, vol. 22, no. 7, pp. 459–461, Apr. 2010.

[19] X. M. Lv *et al.,* "Analysis of vertical radiation loss and far-field pattern for microcylinder lasers with an output waveguide," *Opt. Exp.*, vol. 21, no. 13, pp. 16069–16074, Jul. 2013.

[20] Y. Z. Huang and Y. D. Yang, "Calculation of light delay for coupled microrings by FDTD technique and Padé approximation," *J. Opt. Soc. Amer. A, Opt. Image Sci.*, vol. 26, no. 11, pp. 2419–2426, Nov. 2009.

[21] J. V. Campenhout *et al.,* "Design and optimization of electrically injected InP-based microdisk lasers integrated on and coupled to a SOI waveguide circuit," *J. Lightw. Technol.*, vol. 26, no. 1, pp. 52–63, Jan. 2008.